The Crystal Structure of YdcE, a 4-Oxalocrotonate Tautomerase Homologue from *Escherichia coli*, Confirms the Structural Basis for Oligomer Diversity[†,‡]

Jeffrey J. Almrud,[§] Andrew D. Kern,[§] Susan C. Wang,[||] Robert M. Czerwinski,[||] William H. Johnson, Jr.,[||] Alexey G. Murzin,[⊥] Marvin L. Hackert,*[,§] and Christian P. Whitman*[,||]

Department of Chemistry and Biochemistry and Division of Medicinal Chemistry, College of Pharmacy, The University of Texas, Austin, Texas 78712-1071, and Centre for Protein Engineering, MRC Centre, Hills Road, Cambridge CB2 2QH, U.K.

Received April 8, 2002; Revised Manuscript Received June 6, 2002

ABSTRACT: The tautomerase superfamily consists of three major families represented by 4-oxalocrotonate tautomerase (4-OT), 5-(carboxymethyl)-2-hydroxymuconate isomerase (CHMI), and macrophage migration inhibitory factor (MIF). The members of this superfamily are structurally homologous proteins constructed from a simple $\beta-\alpha-\beta$ fold that share a key mechanistic feature; they use an amino-terminal proline, which has an unusually low pK_a, as the general base in a keto−enol tautomerization. Several new members of the 4-OT family have now been identified using PSI-BLAST and categorized into five subfamilies on the basis of multiple-sequence alignments and the conservation of key catalytic and structural residues. The members of subfamily 5, which includes a hypothetical protein designated YdcE from *Escherichia coli*, are predicted not to form hexamers. The crystal structure of YdcE has been determined to 1.35 Å resolution and confirms that it is a dimer. In addition, YdcE complexed with (*E*)-2-fluoro-*p*-hydroxycinnamate, identified as a potent competitive inhibitor of this enzyme, as well as *N*-(2-hydroxyethyl)-piperazine-*N*′-2-ethanesulfonic acid (HEPES) and benzoate are also presented. These latter crystal structures reveal the location of the active site and suggest a mechanism for the observed YdcE-catalyzed tautomerization reaction. The dimeric arrangement of YdcE represents a new structure in the 4-OT family and demonstrates structural diversity within the 4-OT family not previously reported.

4-Oxalocrotonate tautomerase (4-OT)[1] from *Pseudomonas putida mt-2* catalyzes the isomerization of unconjugated α-keto acids such as 2-oxo-4-hexenedioate (**1**, Scheme 1) to its conjugated isomer 2-oxo-3-hexenedioate (**3**) through the dienol intermediate 2-hydroxy-2,4-hexadienedioate, known commonly as 2-hydroxymuconate (**2**) (*1*, *2*). The gene for 4-OT is found on the TOL plasmid pWW0, and is part of a pathway that degrades aromatic hydrocarbons such as toluene, *m*- and *p*-xylene, 3-ethyltoluene, and 1,2,4-trimethylbenzene (*1*, *2*). Organisms that have the TOL plasmid utilize these compounds as their sole sources of carbon and energy.

Scheme 1

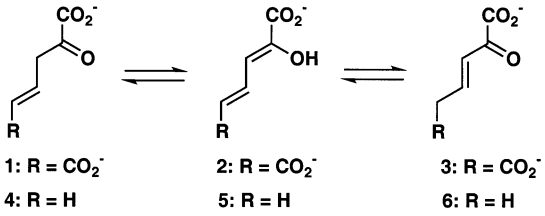

4-OT is a homohexamer composed of unusually small subunits. Each monomer contains 62 amino acid residues and displays a relatively simple $\beta-\alpha-\beta$ fold (Figure 1A) (*3*, *4*). The monomer begins with an amino-terminal proline at the start of a β-strand (β1), followed by an α-helix (α1) and a 3_{10}-helix preceding a second β-strand (β2), and ends with a β-hairpin near the C-terminus (Figure 1A). The 4-OT dimer (Figure 1B) results from antiparallel interactions between the β-sheets and α-helices of two monomers, forming a four-stranded β-sheet with antiparallel α-helices on one side. Three dimers associate to form the hexamer (Figure 1C) by the interactions of the strands of the C-terminal β-hairpins with the edges of the four-stranded β-sheet of neighboring dimers.

The oligomeric arrangement of 4-OT is critical for catalysis because the active sites are located at the dimer

[†] This research was supported by National Institutes of Health Grant GM-41239 to C.P.W. and Robert A. Welch Foundation Grants F-1334 to C.P.W. and F-1219 to M.L.H. S.C.W. is a Fellow of the American Foundation for Pharmaceutical Education.

[‡] The coordinates for the structures described in this paper have been deposited with the Brookhaven Protein Data Bank (entries 1GYJ, 1GYY, and 1GYX).

* To whom correspondence should be addressed. M.L.H.: telephone, (512) 471-1105; fax, (512) 471-8696; e-mail, m.hackert@mail.utexas.edu. C.P.W.: telephone, (512) 471-6198; fax, (512) 232-2606; e-mail, whitman@mail.utexas.edu.

[§] Department of Chemistry and Biochemistry, The University of Texas.

[||] Division of Medicinal Chemistry, The University of Texas.

[⊥] MRC Centre.

[1] Abbreviations: CHMI, 5-(carboxymethyl)-2-hydroxymuconate isomerase; ESI-MS, electrospray ionization mass spectrometry; EMTS, ethyl mercurithiosalicylate; F_o and F_c, observed and calculated structure factors, respectively; FOM, figure of merit; HEPES, *N*-(2-hydroxyethyl)-piperazine-*N*′-2-ethanesulfonic acid; HPLC, high-pressure liquid chromatography; IPTG, isopropyl β-D-thiogalactoside; Kn, kanamycin; LB, Luria-Bertani medium; MIF, macrophage migration inhibitory factor; MIR, multiple isomorphous replacement; NCS, noncrystallographic symmetry; NMR, nuclear magnetic resonance; 4-OT, 4-oxalocrotonate tautomerase; PCR, polymerase chain reaction; rms, root-mean-square; SDS−PAGE, sodium dodecyl sulfate−polyacrylamide gel electrophoresis.

10.1021/bi020271h CCC: $22.00
Published on Web 08/21/2002

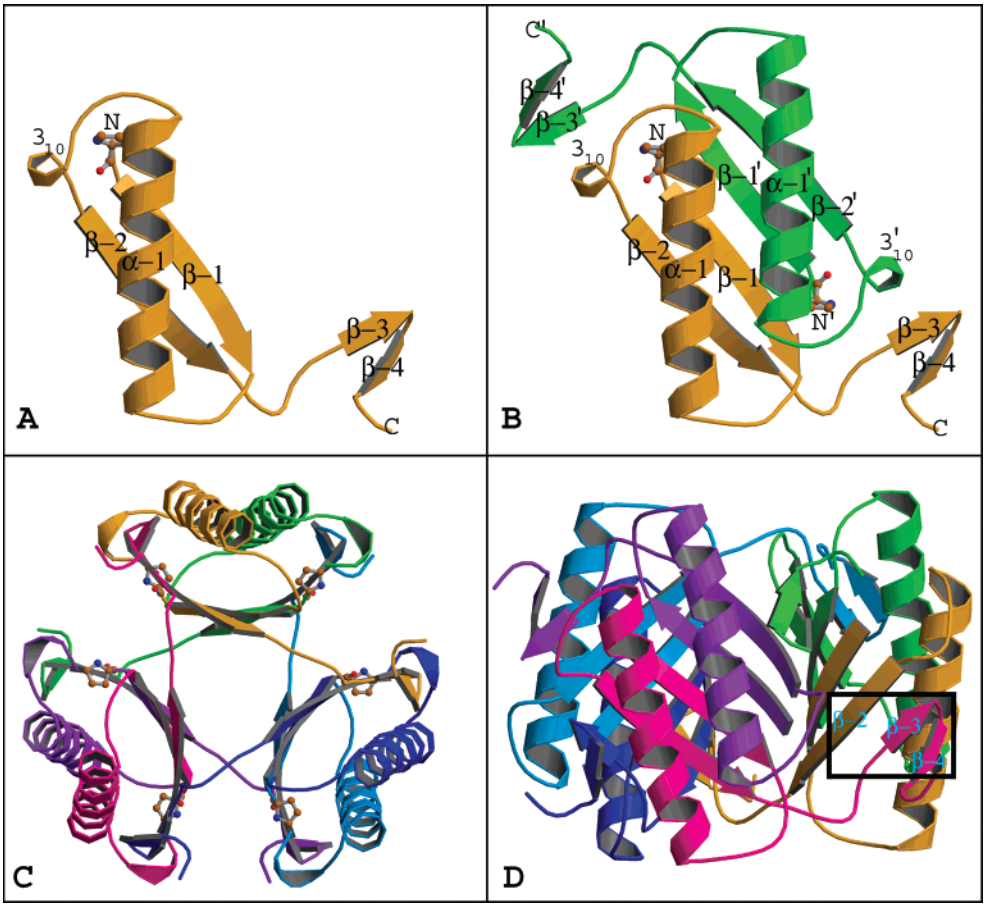

FIGURE 1: Ribbon diagrams depicting (A) the 4-OT monomer, (B) a side view of the 4-OT dimer, (C) a top view of the 4-OT hexamer, and (D) a side view of the 4-OT hexamer (*3*). The catalytic amino-terminal proline is shown in panels A−C to identify the location of the active sites at the dimer interfaces. Dimer formation generates a four-stranded β-sheet with flanking antiparallel helices. The β-hairpin is boxed in panel D to highlight the interaction of β-3 and β-4 of one dimer with β-2 of a neighboring dimer. This figure was produced using RASTER3D (*5*) and MOLSCRIPT (*6*).

Scheme 2

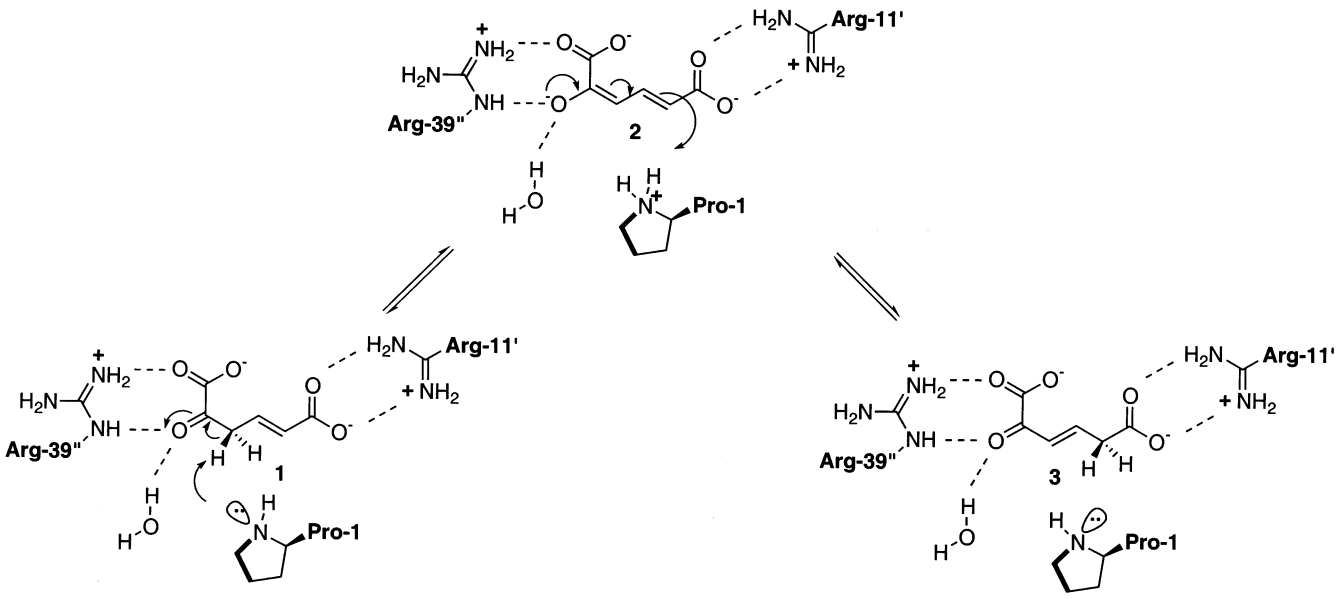

interfaces (*4*). Thus, Pro-1 of one monomer functions as the catalytic base (*4*, *7*−*11*), while Arg-11′ from an adjacent monomer but within the same dimer plays a role in both binding and catalysis (*12*) (Scheme 2).[2] It binds the C-6 carboxylate group (of **1**) and serves as an electron sink to draw electron density to the C-5 position to allow protonation. Arg-39″, from the neighboring dimer, binds one oxygen

[2] The unprimed, primed, and doubly primed residues refer to different subunits within the 4-OT homohexamer and the YdcE dimer.

Scheme 3

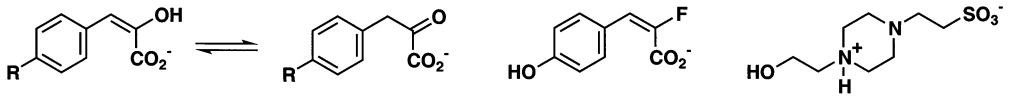

7: R = H **8: R = H** **11** **12**
9: R = OH **10: R = OH**

of the C-1 carboxylate group, and, along with an ordered water molecule, polarizes the carbonyl group of **1**, which facilitates proton abstraction at C-3 by Pro-1. Pro-1 is able to function as a base under physiological conditions because it has a pK_a of ~6.4 (*8*). The lowered pK_a of the proline is due primarily to its position in a hydrophobic pocket of the active site, which is maintained, in part, by Phe-50 (*13*).

We have now identified several 4-OT homologues in organisms ranging from *Escherichia coli* to the thermophile *Archaeoglobas fulgidus.* These short, chromosomal sequences (61−81 amino acids) absolutely conserve the amino-terminal proline, and generally have an aromatic amino acid at the Phe-50 position and a glycine at position 54 to conserve the characteristic $\beta-\alpha-\beta$ motif. Many but not all of these homologues have a GXGG sequence (residues 51−54 using the 4-OT numbering system), following the aromatic amino acid. The XGG sequence is found in a type II β-hairpin loop connecting two short β-strands. Amino acid residues with small side chains are clearly favored at position 54 to produce the tight turn of the β-hairpin. The β-hairpin is critical for hexamer formation as it interacts with and extends the core sheet structure of the adjacent dimers. The bulk of the aromatic ring of Phe-50 provides a platform that supports the GXGG region so it can fully extend and "reach" into the neighboring dimer (Figure 1D).

Interestingly, two "hypothetical proteins" designated YdcE in *E. coli* and XF1725 in *Xylella fastidiosa* consisting of 76 and 81 amino acids, respectively, do not have the GXGG sequence or a structural equivalent. Instead, the aromatic amino acid is followed by a nine-amino acid stretch that is predicted to be α-helical in nature. This observation prompted two questions. First, does the presumed helix exist, and if so, does this change the oligomeric state of the enzyme? Second, if there is a change in the quaternary structure, what effect does this perturbation have on catalysis and the function of the enzyme?

To address these questions, we cloned, overexpressed, and purified the *E. coli* homologue and characterized its tautomerase activity with 2-hydroxy-2,4-pentadienoate (**5**, Scheme 1), and the enol isomers of phenylpyruvate (**7**, Scheme 3) and (*p*-hydroxyphenyl)pyruvate (**9**). We have also determined crystal structures of the native enzyme and three inhibitor complexes: (*E*)-2-fluoro-*p*-hydroxycinnamate (**11**, Scheme 3), a potent competitive inhibitor, as well as *N*-(2-hydroxyethyl)piperazine-*N*′-2-ethanesulfonic acid (HEPES, **12**) and benzoate. These structures show that the YdcE homologue is a dimer, instead of the usual hexamer. This arrangement represents a new structure in the 4-OT family that uses the $\beta-\alpha-\beta$ fold as its building block and demonstrates structural diversity within the 4-OT family not previously reported. The YdcE complexes also provide a structural basis for the enzymatic activity of YdcE and the potency of **11** as an inhibitor.

EXPERIMENTAL PROCEDURES

Materials. All reagents, buffers, and solvents were obtained from either Aldrich Chemical Co. or Sigma Chemical Co., with the exception of (*E*)-2-fluoro-*p*-hydroxycinnamate (**11**), which was synthesized according to a literature procedure (*14*). Tryptone and yeast extract were obtained from Difco (Detroit, MI). The YM-3 ultrafiltration membranes were obtained from Millipore (Bedford, MA). Isopropyl β-D-thiogalactoside (IPTG) and thin-walled PCR tubes were obtained from Ambion, Inc. (Austin, TX). The syntheses of 2-hydroxymuconate (**2**, Scheme 1) and 2-hydroxy-2,4-pentadienoate (**5**, Scheme 1) are described elsewhere (*15*, *16*). The expression vector pET24a(+) was obtained from Novagen, Inc. Restriction enzymes, T4 DNA ligase, low-melting point agarose, the Wizard PCR Preps DNA purification kit, and the Wizard Plus Minipreps DNA Purification System were obtained from Promega Corp. (Madison, WI). The Geneclean II kit was purchased from Bio 101, Inc. (La Jolla, CA). The PCR was carried out using the PCR Reagent system from Promega Corp. or the GeneAmp kit from Perkin-Elmer-Cetus (Norwalk, CT). Oligonucleotides for site-directed mutagenesis and DNA sequencing were synthesized by Oligos Etc. Inc. (Wilsonville, OR).

Strains. *E. coli* strain JM109 was obtained from Promega Corp. and was used for transformation of ligated plasmids. *E. coli* strain BL21(DE3)pLysS was obtained from Novagen and used for expression of the recombinant proteins. The *E. coli* K12 strain (ATCC 29425) was obtained from American Type Culture Collection (Rockville, MD). Cells for general cloning and expression were grown in LB medium supplemented with kanamycin (50−100 μg/mL). The composition of LB medium is described elsewhere (*17*).

General Methods. Techniques for restriction enzyme digestions, ligation, transformation, and other standard molecular biology manipulations were based on methods described elsewhere (*17*). Genomic DNA from *E. coli* K12 was isolated following a published procedure (*18*). DNA sequencing was carried out at the University of Texas Sequencing Facility. Kinetic data and UV absorbance readings were obtained on a Hewlett-Packard 8452A diode array spectrophotometer. The kinetic data were fitted by nonlinear regression data analysis using the Grafit program (Erithacus Software Ltd., Staines, U.K.) obtained from Sigma Chemical Co. HPLC was performed on a Waters system using either a Bio-Gel Phenyl 5-PW hydrophobic column or a Pharmacia Superose 12 (HR 10/30) gel filtration column. Protein was analyzed by tricine sodium dodecyl sulfate−polyacrylamide gel electrophoresis (SDS−PAGE) under denaturing conditions on 17.5% gels on a vertical gel electrophoresis apparatus obtained from Gibco (*19*). Protein concentrations were determined using the method of Waddell (*20*).

Construction of the Expression Vector for the Production of YdcE. Two oligonucleotides (5′-GAAGGAGATATACATATGCCATACGTAACTGTCAAA-3′ and 5′-GAGCTCGAATTCGGATCCCTATTATTCCATATCGTCCAG-3′) were synthesized for the amplification of the YdcE gene from *E. coli*. The first primer contains an *Nde*I restriction site (underlined) followed by 18 bases corresponding to the coding sequence of the YdcE gene, whereas the second primer contains a *Bam*HI restriction site (underlined) followed by 21 bases corresponding to the complementary sequence of the YdcE gene. The PCR was carried out in a Perkin-Elmer DNA thermocycler 480 using the two synthetic primers, genomic DNA, and the PCR reagents supplied in either the PCR Reagent system or the Perkin-Elmer-Cetus GeneAMP kit following a protocol described elsewhere (*10*). The resulting gel-purified DNA fragment and the pET24a-(+) vector were digested with *Nde*I and *Bam*HI restriction enzymes, purified, and ligated using T4 DNA ligase following a previously described protocol (*10*). Aliquots of the resulting mixture were transformed into competent *E. coli* JM109 cells and grown on LB/Kn (100 μg/mL) plates at 37 °C. Single colonies were chosen at random and grown in liquid LB/Kn medium (50−100 μg/mL). The newly constructed plasmid was isolated and the gene sequenced. Subsequently, the plasmid was transformed as described elsewhere into *E. coli* strain BL21(DE3)pLysS for protein expression (*10*).

Overexpression and Purification of the Recombinant Enzyme. A single colony of the expression strain containing the plasmid was used to inoculate 25 mL of LB/Kn medium (50−100 μg/mL). After overnight growth at 37 °C, 3 mL of the culture was used to inoculate 500 mL of LB/Kn medium (50−100 μg/mL) in a 2 L Erlenmeyer flask. Cultures were grown to an OD_{600} of ∼0.6−0.8 at 37 °C with vigorous shaking and then induced with IPTG (0.5 mM final concentration). Incubation was continued for 4 h at 37 °C. Cells were harvested by centrifugation (7000*g* for 12 min) and stored at −80 °C. Typically, 3 L of culture grown under these conditions yields 9.5 g of cells.

The enzyme was purified to near homogeneity (>95% as assessed by SDS−PAGE) by a modification of a previously published procedure (*13*). YdcE eluted from the Bio-Gel Phenyl hydrophobic column near the end of the ammonium sulfate gradient (∼0.5−0 M). The active fractions were pooled, concentrated, and loaded onto a G-75 gel filtration column (2.5 cm × 100 cm) equilibrated with 20 mM sodium phosphate buffer (pH 7.3). At a flow rate of 0.5 mL/min, the protein eluted after 12 h and was collected in 10 mL fractions. Typically, the yield of purified enzyme per liter of culture is 50 mg. For crystallization studies, protein solutions were exchanged into 50 mM sodium phosphate buffer (pH 7.3) or 50 mM HEPES buffer (pH 7.3). The native molecular mass was estimated by size exclusion chromatography on a Superose 12 column. The enzyme was chromatographed in 100 μL portions (∼8.3 mg/mL) on the gel filtration column equilibrated with 10 mM ethylenediamine buffer (pH 7.3) at a flow rate of 0.40 mL/min. Protein was monitored at 254 nm. The protein eluted at ∼35 min, corresponding to a native molecular mass of 29 400 Da. The estimated pI of YdcE is 4.7 versus an estimated pI of 7.9 for 4-OT.

Mass Spectrometry. The monomeric mass of the purified enzyme was determined by electrospray ionization mass spectrometry (ESI-MS) using a LCQ Finnigan octapole electrospray mass spectrometer. The samples for ESI-MS were prepared and analyzed as previously described (*12*). The observed monomeric molecular mass (MH^+) for YdcE is 8540 Da (calcd 8542 Da).

Sequence Analysis. An iterative PSI-BLAST search of the NCBI nonredundant database was performed using the amino acid sequence of 4-OT from *P. putida* (*19*) as the query sequence (*21*). The databases were searched with the "NR" option (all nonredundant GenBank CDS translations + PDB + SwissProt + PIR + PRF). 4-OT homologue amino acid sequences (not including MIF-related sequences in the superfamily) were selected on the basis of significance scores, redundancies eliminated, and the remaining sequences subjected to multiple-sequence alignment analysis using a version of the CLUSTALW multiple-sequence alignment routines in the computational tools at the EMBL Web site (*22*). The resulting amino acid sequence alignment was examined, and small adjustments were made as deemed appropriate based on our understanding of the structure. The resulting sequence alignments were subjected to pairwise alignment scoring to create a matrix for PHYLIP (the PHYLogeny Inference Package) for inferring phylogenies (evolutionary trees) (*23*). The PHYLIP package is available over the Internet as part of the EMBL Web site. The methods available in the package include parsimony, distance matrix, and likelihood methods, including bootstrapping and consensus trees.

Kinetic Studies of YdcE. The ketonization of **7** to **8** (Scheme 3) was monitored by following the disappearance of **7** at 288 nm ($\epsilon = 18\,000\ M^{-1}\ cm^{-1}$), and the ketonization of **9** to **10** (Scheme 3) was monitored by following the disappearance of **9** at 292 nm ($\epsilon = 20\,800\ M^{-1}\ cm^{-1}$) (*24*). The conversion of **5** to **4** was monitored by following the disappearance of the dienol at 265 nm, as described elsewhere (*25*). The formation of **3** from **2** was assessed at 236 nm as described previously (*15*). The kinetic studies were carried out in 20 mM NaH_2PO_4 buffer (pH 7.3).

Inhibition Studies of YdcE. The reversible competitive inhibition of YdcE was examined using (*E*)-2-fluoro-*p*-hydroxycinnamate (**11**), HEPES (**12**), and benzoic acid. For each experiment, a quantity of YdcE (37.5 μL of a 27.3 mg/mL solution) was added to 150 mL of assay buffer [20 mM sodium phosphate buffer (pH 7.3)] and incubated for 1 h. Subsequently, an aliquot of inhibitor from a stock solution was added to a 15 mL portion of the diluted enzyme solution to yield the approximate final inhibitor concentration. After 5−10 min, aliquots (1 mL) of the resulting solution were removed and assayed using 12 concentrations (from 10 to 150 μM) of the enol isomer of phenylpyruvate (**7**). The final concentrations of **11** ranged from 0 to 120 μM, and were diluted from a 100 mM stock solution, which was made in ethanol using the free acid. The final concentrations of HEPES ranged from 0 to 40 mM, and were diluted from a 1 M stock solution, which was made in water using the hemisodium salt. The final concentrations of benzoic acid ranged from 0 to 10 mM, and were diluted from a 1 M stock solution, which was made up in ethanol. The pH of the assay solution was adjusted to 7.3 when necessary. The kinetic data were fitted by nonlinear regression data analysis using

Table 1: Crystal and Diffraction Data for Native YdcE and the YdcE·**11** Complex

	YdcE	YdcE·**12**/ benzoate	YdcE·Pt	YdcE·Hg	YdcE·**11**
space group	$P2_12_12_1$	$P2_12_12_1$	$P2_12_12_1$	$P2_12_12_1$	$P2_12_12_1$
cell constants					
a (Å)	37.3	44.6	45.0	45.0	44.7
b (Å)	63.8	46.5	47.3	47.3	46.7
c (Å)	71.3	75.7	75.6	76.6	76.2
camera length (mm)	170	72	150	150	72
oscillation angle (deg)	2.0	1.5	2.0	2.0	2.0
exposure time (min)	30	15	5	5	18
no. of images	124	110	120	60	46
resolution range (Å)					
overall	30−2.1	25−1.35	25−2.0	25−2.0	25−1.35
highest-resolution bin	2.18−2.10	1.39−1.35	2.06−2.0	2.06−2.0	1.39−1.35
total no. of reflections	169053	156715	152857	67500	276503
total no. of unique reflections	10344	35377	11455	11597	36652
total no. of R_{free} reflections	491	979	−	−	1678
R_{merge} (%)					
overall	9.2	3.6	11.5	5.6	3.7
highest-resolution bin	43.5	17.5	31.9	9.7	15.9
completeness (%)					
overall	99.7	87.4	100.0	96.1	91.4
highest-resolution bin	99.1	33.0	100.0	96.1	35.0
no. of heavy atom sites	−	−	2	4	−

MIR Phasing: Mean Figure of Merit vs Resolution

resolution (Å)	7.0	4.5	3.5	3.0	2.6	2.4	2.2	2.1	overall
FOM	0.64	0.59	0.55	0.54	0.54	0.52	0.46	0.38	0.51

the equation for competitive inhibition provided by the Grafit program.

Crystallization. Crystals of YdcE were obtained from protein exchanged into 50 mM sodium phosphate buffer (pH 7.3) as follows. Hanging drops were set up at 4 °C and consisted of 5 μL of protein (20 mg/mL) and 5 μL of well solution [40% (w/v) sodium citrate buffer (pH 8.5)], with 500 μL of solution in each well of the plate. Data-quality crystals grew to an approximate size of 0.6 mm × 0.6 mm × 0.2 mm within 4 weeks. The space group of the crystals is $P2_12_12_1$ with the following unit cell dimensions: $a = 37.3$ Å, $b = 63.8$ Å, and $c = 71.3$ Å. If it is assumed that a dimer is present in the asymmetric unit, the Matthews coefficient is 2.5 Å^3/Da (*26*), and the solvent content is approximately 51%.

Crystals of YdcE were also obtained from protein exchanged into 50 mM HEPES buffer (pH 7.3) as follows. The crystallization conditions were initially identified using the Hampton's Crystal Screen II kit. These conditions were refined, and high-resolution, data-quality crystals were subsequently grown at 4 °C using the sitting-drop method, where 15 μL of the protein [25 mg/mL YdcE in 50 mM HEPES buffer (pH 7.3)] was mixed with 5 μL of 40% (w/v) sodium citrate buffer (pH 6.5). Crystals grew to a mature size of 0.4 mm × 0.4 mm × 0.5 mm within 3 weeks. The space group of the crystals is $P2_12_12_1$ with the following unit cell dimensions: $a = 44.7$ Å, $b = 46.7$ Å, and $c = 76.2$ Å. If it is assumed that a dimer is present in the asymmetric unit, the Matthews coefficient is 2.87 Å^3/Da, and the solvent content is approximately 56.8%. The YdcE crystals were complexed with **11** by soaking in 40% (w/v) sodium citrate buffer (pH 6.5) containing 10 mM **11** for 60 min at 4 °C.

Data Collection. Diffraction data were collected to 2.1 Å resolution from a single crystal of YdcE in 50 mM sodium phosphate buffer on a MAR345 detector installed on a Rigaku RU200H rotating anode X-ray generator equipped with focusing mirrors. The crystal was mounted in a cryoloop directly from the mother liquor, and then flash-cooled to −175 °C by immersing the loop directly into liquid nitrogen. Crystals were kept at −165 °C during data collection using an Oxford Instruments cryo-cooling device.

Diffraction data were collected to 1.35 Å resolution from single crystals of YdcE in 50 mM HEPES buffer and of the YdcE·**11** complex using an RAXIS-IV image plate detector installed on the same Rigaku RU200H rotating anode X-ray generator as described above. The crystals were mounted in the same fashion as the other YdcE crystal, but kept at −165 °C during data collection using a Molecular Structures Corp. cryo-cooling device. All diffraction data sets were processed using the programs DENZO and SCALEPACK (*27*). Intensities were converted to structure factors using TRUNCATE of the CCP4 version 4.0 suite of crystallographic programs (*28*), and an R_{free} set was assigned using the CCP4 program FREERFLAG. The crystal and data collection statistics are summarized in Table 1.

Structure Determination. The structure of YdcE (exchanged in HEPES buffer) was determined by the multiple-isomorphous replacement (MIR) method using platinum and mercury derivatives. The platinum derivative was produced by soaking the crystals in a solution of 10 mM K_2PtCl_4 and 40% (w/v) sodium citrate buffer (pH 6.5) for 20 h. The mercury derivative was obtained by soaking crystals in 10 mM ethyl mercurithiosalicylate (EMTS) and 40% (w/v) sodium citrate buffer (pH 6.5) for 12 h. The program SOLVE (*29*) was used to produce initial phases to 2.0 Å (see Table 2), and wARP (*30*) was used to produce a map to 1.35 Å resolution, with a weighted *R*-factor of 15.5%. In mode "warpNtrace", the program wARP successfully built the YdcE main chain plus 621 additional atoms, yielding a starting model with an *R*-factor of 18.6% and an R_{free} of 22.2%.

Table 2: Structural Refinement Statistics for Native YdcE and Complexes

	YdcE	YdcE·**12**/ benzoate	YdcE·**11**
resolution range (Å)			
overall	30.0−2.1	25.0−1.35	25.0−1.35
highest-resolution bin	2.18−2.10	1.39−1.35	1.39−1.35
no. of protein atoms modeled	1197	1192	1192
no. of water molecules modeled	151	290	285
no. of inhibitor atoms	−	24	26
Ramachandran plot			
residues in core (%)	92.8	96.4	96.4
residues in allowed region (%)	7.2	3.6	3.6
residues in disallowed region (%)	0.0	0.0	0.0
deviation in bond distances (Å)	0.008	0.009	0.009
deviation in bond angles (deg)	1.4	1.5	1.5
average thermal factor (Å^2)			
protein	24.3	6.2	7.9
solvent	34.4	19.1	24.4
inhibitor	−	13.5	18.4
R-factor (%)			
overall	22.5	14.2	15.1
highest-resolution bin	30.2	22.6	25.4
R_{free} (%)			
overall	26.2	16.4	17.3
highest-resolution bin	32.9	25.5	25.6

The structure of the YdcE·**11** complex was determined by molecular replacement techniques using a partially refined, 1.5 Å resolution model of YdcE obtained as described above. The molecular replacement model was initially rigid-body fit against data collected for the YdcE·**11** complex, using the CCP4 program AMORE (*31*). Phases were initially calculated to 1.35 Å resolution, and then improved using the program wARP. The resulting wARP electron density map, calculated to 1.35 Å resolution, showed unambiguous electron density for the inhibitor. The YdcE model was then refit to the wARP (F_o; α_{wARP}; FOM_{wARP}) electron density map, followed by crystallographic refinement as described below.

The structure of native YdcE from crystals grown in phosphate buffer was determined by molecular replacement using the CCP4 suite program MOLREP. The search model for the rotation and translation function was the refined crystal structure of YdcE from crystals grown in HEPES buffer. The resulting molecular replacement solution was unambiguous with an initial correlation coefficient of 61.5%, and an *R*-factor of 37.6%.

Structure Refinement. The models were refined by iterations of computer-based minimization, followed by manual fitting of the model to electron density maps using Swiss PDB Viewer (*32*) and the program O (*33*). The structures of YdcE (in HEPES) and the YdcE·**11** complex were refined from 25 to 1.35 Å resolution using REFMAC version 4.0 (*34*) with a maximum likelihood target function, and bulk-solvent correction for all rounds of refinement. The decrease in the R_{free} value was used to direct the refinement procedure. Manual rebuilding was carried out using σ-A weighted [$2F_o - F_c$] electron density maps, with $F_o - F_c$ maps being used to monitor the model rebuilding process. A water-picking routine (using the CCP4 programs REFMAC and ARP) was used to place ordered solvent molecules in [$2F_o - F_c$] and $F_o - F_c$ electron density maps. The addition of partial structure factor contributions from hydrogen atoms, bulk solvent correction, anisotropic temperature factor refinement, and multiple conformations were each accompanied by a reduction in the R_{free} value. The refinement statistics are summarized in Table 2.

The native structure of YdcE was refined using CNSsolve version 1 (*35*). Multiple rounds of refinement were carried out using simulated annealing, energy minimization, and individual *B*-factor refinement. Solvent molecules were picked using a CNSsolve water picking script. A decrease in the R_{free} value was observed with the release of NCS restraints, and the addition of water molecules. The refinement statistics are summarized in Table 2.

RESULTS

Sequence Analysis. Four iterations of PSI-BLAST resulted in more than 50 sequences judged to be homologues based on significance scores. These sequences included 4-OT homologues, the α- and β-subunits of *trans*-3-chloroacrylic acid dehalogenase from *Pseudomonas pavonaceae* (*36*), and several sequences belonging to the macrophage migration inhibitory factor (MIF) family. After removal of the sequences corresponding to the MIF family and the 4-OT redundancies, the 38 remaining sequences were subjected to multiple-sequence alignment using CLUSTALW (*22*). After some additional minor adjustments, the results identify at least five 4-OT subfamilies (Table 3), which are grouped on the basis of the conservation of key structural and catalytic residues (shown in bold letters in Table 3). The analysis suggests that the homologues in subfamilies 1−4 will form hexamers while those in subfamily 5 will not. This prediction is based on the observation that the homologues in subfamilies 1−4 contain the four highly conserved structural residues, Lys-16, Glu-44, Phe-50, and Gly-54. Lys-16 from the first turn of the α-helix (α-1) and Glu-44 (from the second β-strand) form an internal salt bridge that appears to be crucial for stabilizing the helix−sheet interaction in the β−α−β motif. More importantly, the aromatic residue (Phe-50) and the subsequent β-hairpin ending with Gly-54 are critical for dimer−dimer interactions and further stabilize hexamer formation, as noted earlier. With regard to the three key catalytic groups (Pro-1, Arg-11, and Arg-39) found in 4-OT and the homologues comprising subfamily 1, only Pro-1 is conserved in the other subfamilies. In subfamily 2, Arg-39 is replaced with a histidine. In subfamily 3, Arg-39 is replaced with a hydrophobic residue (Val or Phe). Arg-11 is also missing, but a conserved lysine (Lys-33) is now present. The sequences in this subfamily retain Pro-1, three key structural residues (Lys-16, Glu-44 or Asp-44, and Gly-54), and generally the aromatic residue in the Phe-50 position, but none of the other active site residues. The characteristics of subfamily 4 are not as well defined as those of the other subfamilies and may require further subdivision as new sequences and further structural studies are reported. Finally, subfamily 5 (including YdcE) has the N-terminal proline, the amino acid residues equivalent to Arg-11 (Arg-10) and Lys-16 (Lys-17), and an aromatic residue equivalent of Phe-50 (Trp-51). However, the aromatic residue is not followed by the GXGG sequence characteristic of the β-hairpin that enables hexamer formation. This subfamily classification is supported further by the results of pairwise sequence alignment scoring to create a matrix for generating an evolutionary tree using PHYLIP (*23*) as shown in Figure 2. Boxes that approximate the five subfamilies as described above are superimposed on the tree.

Table 3: Subfamilies of the 4-OT Sequence Homologues

Probable Hexamers		
1.	bbbbbbb hhhhhhhhhhhhhhhhhh bbbbbbb bbb bbb hhh + + + + + + + +	
Pseudomonas putida XylH[a]	**P**IAQIHIL-E----**GR**---SDEQ**K**ETLIREVSEAISRSLDAPLTSV**R**VIITE**M**AKGH-**FGIGG**ELASKVRR	gi|18150922
Pseudomonas stutzeri NahJ	**P**IAQIHIL-E----**GR**---SDEQ**K**ETLIREVSEAISRSLDAPLTSV**R**VIITE**M**PKVH-**FGIGG**ESAKAIGR	gi|4104773
Pseudomonas sp. DmpI	**P**IAQLYII-E----**GR**---TDEQ**K**ETLIRQVSEAMANSLDAPLERV**R**VLITE**M**PKNH-**FGIGG**EPASKVRR	gi|1352275
Pseudomonas putida NahJ	**P**IAQLYIL-E----**GR**---SDEQ**K**ETLIREVSEAMSRSLDAPIERV**R**VIITE**M**PKNH-**FGIGG**EPASKLNR	gi|4235478
Pseudomonas putida TdnL	**P**FAQIYMI-E----**GR**---TEAQ**K**KAVIEKVSQALVEATGAPMANV**R**VWIQE**V**PKEN-**WGIAG**VSAKELGR	gi|14715457
Comamonas testosteroni AphI	**P**FAQIYML-E----**GR**---SEEQ**K**KAVIEKVTRALVEAVGAPSANV**R**VWIH**D**VPKEN-**WGIAG**VSAKELGR	gi|6624277
Ralstonia solanacearum Rsp0893	**P**LIQVTLI-E----**GR**---TMEA**K**AALIGSLTQAAVATLGAPRESV**R**VIIQE**V**PAAH-**WGVAG**VPKSAAKEPPRDSKA	gi|17549114
Novosphingobium aromaticivorans XylH	**P**IIEVNLF-E----**GR**---PPEA**K**ERLIKALTDAAIDAIGAPRESV**R**VILRE**M**APAH-**FAVGG**LSFAAKAAAAAAAQPRVEEDWSNEN	gi|10956975
Sphingomonas chungbukensis PhnL	**P**IIEVNLL-E----**GR**---PPEA**K**ERLIRALTDAAIGAIGAPRESV**R**VILRE**M**DPAH-**F**AV**GG**VSFAAKAAAAQPRVEEDWSNEA	gi|4091976
2.		
Staphylococcus aureus SAV1363	**P**IVNVKLL-E----**GR**---SDEQLKNLVSEVTDAVEKTTGANRQAI**H**VVIEE**M**KPNH-**YGVAG**VRKSDQ	gi|15924353
Bacillus halodurans BH3814	**P**IVTVKFL-E----**GR**---SDEQ**K**RALVERVTEAVAETIQANPEKI**H**VVLEE**M**RKDH-**YGVAG**KRISDQ	gi|15616376
Listeria innocua Lin2709	**P**FVTIQFL-E----**GR**---SDDQ**K**KALVSEVTDVVSKNLKAPKENI**H**VILEE**M**KKTD-**YGVGG**VRKSDI	gi|16801770
Listeria monocytogenes Lmo2564	**P**FVTIQFL-E----**GR**---TDDQ**K**KALVSEVTEVVSKNLKAPKENI**H**VILEE**M**KKTD-**YGVGG**VRKSDI	gi|16804602
Streptococcus pyogenes Spy1139	**P**FVTIDLF-E----**GR**---SQEQ**K**NQLAREVTEVVSRIAKAPKENI**H**VFIND**M**PEGT-**Y**YPQ**GG**EMKQKS	gi|15675116
Streptococcus thermophilus 4-OT	**P**FVKIDLF-E----**GR**---SEEQ**K**IELAREVTEVVSRVAKAPKEAI**H**VFIND**M**PEGT-**YYPHGG**EMKKKN	gi|12054924
Streptococcus pneumoniae SP1017	**P**FVRIDLF-E----**GR**---TLEQ**K**KALAKEVTEAVVRNTGAPQSAV**H**VIIND**M**PEGT-**Y**FPQ**GG**EMRTK	gi|15900888
Lactococcus lactis XylH	**P**YVHVELF-E----**GR**---TVEQ**K**AIIAKEITESISKHAGAPTSAI**H**VIFND**L**PEGM-LYQ**GG**EMKKKK	gi|15672556
Bacillus subtilis YwhB	**P**YVTVKML-E----**GR**---TDEQ**K**RNLVEKVTEAVKETTGASEEKIVVFIEE**M**RKDH-**YAVAG**KRLSDME	gi|16080806
3.		
Helicobacter pylori HP0924	**P**FINIKLVPE--NGGP---TNEQ**K**QQLIEGVSDLMVKVLN**K**NKASIVVIID**E**VDSNN-**YGLGG**ESVHHLRQKN	gi|15645540
Campylobacter jejuni Cj1255	**P**FVNIRITKE--NGEP---TTEQ**K**QELIAGVTDLLAKVLN**K**NKSSTVVIID**E**IDTDN-**YGLGG**KSITQARKEKS	gi|15792579
Neisseria meningitidis NMB1474	**P**YVNIKVTGG--KEAP---TAAQ**K**AELIGGVTELLARVLG**K**NPETTVVVID**E**VDTDN-**WGIGG**KSVSERRKEGR	gi|15677328
Yersinia pestis YPO3989	**P**YVNIKITREG-------ATAEQ**K**KQLIAGVTQLLVDTLG**K**NPATTVVVID**E**VETDN-**WGIGG**RSVTDLRQSS	gi|16124116
Erwinia chrysanthemi YkdK	**P**FVNIRITKDG-------VTAEQ**K**KQLIAGVTQLLVDTLG**K**NPATTVVIID**E**VETDN-**WGIGG**ESVTERRQQAHDRKHNV	gi|1176508
Campylobacter jejuni Cj0270	**P**LVNIKLAKPS-------LSKEQ**K**AELIADITELLSTKYN**K**SKERVVVVLE**D**VENYD-**IGFGG**ESVEAIKAKASK	gi|15791641
Caulobacter crescentus CC2975	**P**YVNIQVTREG-------VTREQ**K**ARLIDGVTTLLAEVLG**K**DPNTTFVVIE**E**VALEN-**WGVGG**LPVEAYRARKRPAAT	gi|16127205
Sinorhizobium meliloti SMb20209	**P**IVTVQVTREGSAP**GR**NSVTAEE**K**AAIIKGVSEVLLDVLN**K**PLESTYVVIE**E**VELDN-**WGWGG**FPTVQFRRQRAETARS	gi|16263950
4.		
Archaeoglobus fulgidus AF0669	**P**VLIVYGP---------KLDVGK**K**REFVERLTSVAAEIYGMDRSAITILIH**E**PPAEN-VG**VGG**KLIADRERE	gi|11498277
M. thermoautotrophicum MTH1606	**P**VIQINCN---------ELTREK**K**RELVKRITEVSSEIMGLPESTITVLIR**E**FPPEM-**WG**LEVHSSVTGSEWFLMGVSPR	gi|15679601
Streptomyces coelicolor SCD31.07	**P**FAHFKVP-------AGTLSAED**K**KKIVERTTDLYAEIYGERARPTTVVLV**D**EVPDG**GWG**VAG**N**VLTAAMLNGDG	gi|7321272
Mesorhizobium loti msl4326	**P**FVNIRIVKE-----VIAADPAG**K**KADIAKKVTAAIMEATGLGNDDVWVVF**E**EVNARD**WYVGK**TDVETLRKG	gi|13473656
Ralstonia solanacearum RSc0807	**P**TFHIEMF-E----**GR**---SADQ**K**RKLVEEVTRVTCETLGCAPGAVDIIIA**E**VKREN-**WATGG**VLWSEQK	gi|17545526
Nostoc PCC7120 asr0697	**P**FVTVKIA-R----**GH**---SIEK**K**RHLVEAITNALVTALDTKPEWITIHID**E**FEREN-**WAVNG**ILHCDRHRGRHDETGR	gi|17228192
Ralstonia solanacearum RSp1151	**P**VVRVSWF-E----**GK**---DAKA**K**KAVAAEITDSIVKHAGTDPKYIYVIF**E**DIKPSD-**WAGAG**RLYGEEPGTP	gi|17549372
Mesorhizobium loti msl1978	**P**FANIKLP-------QAALSKAQ**K**EDLIHRTTAMFVDFFGEGVRPTTMVLV**E**EVADGG**YG**RADEVFVIPEAYRAKE	gi|13471867
Pseudomonas pavonaceae CaaD1 (α)	**P**MISCDMR-Y----**GR**---TDEQ**K**RALSAGLLRVISEATGEPRENIFFVIR**E**GSGIN-**F**VEH**G**EHLPDYVPGNANDKALIAKLK	gi|10637969
Pseudomonas pavonaceae CaaD2 (β)	**P**FIECHIA-T----**GL**---SVAR**K**QQLIRDVIDVTNKSIGSDPKIINVLLV**E**HAEAN-MSISG**R**IHGEAASTERTPAVS	gi|10637970
Probable Dimers		
5.	bbbbbbb hhhhhhhhhhhhhhhhhh bbbbbbb hhhhhhhhhh	
Escherichia coli YdcE	**P**HIDIKCF------PREL-DEQQ**K**AALAADITDVIIRHLNSKDSSISIALQQIQPES-**W**-QAIWDAEIAPQMEALIKK**PGY**SMNA	gi|16129420
Xylella fastidiosa XF1725	**P**HIIVKIA-E----**GR**---SQPL**K**QELADRLAATMMDVLGLDSSAVSVAVE**D**VPMQD-**WM**QQVYGPDIETAGERLLKR**PGY**GQLASPPEE	gi|15838326

[a] Species name, gene name, amino acid sequence, gene identifier.

Table 4: Kinetic Parameters for YdcE[a]

substrate	k_{cat} (s^{-1})	K_m (μM)	k_{cat}/K_m (M^{-1} s^{-1})
5	70 ± 13	220 ± 60	3.2×10^5
7	25 ± 2.0	205 ± 20	1.2×10^5
9	2.2 ± 0.2	180 ± 20	1.2×10^4

[a] The steady-state kinetics parameters were determined at 23 °C and pH 7.3. Errors are standard deviations.

Kinetic Studies of YdcE. Several enol and dienol compounds, which are substrates for other members of the tautomerase superfamily, were examined as potential substrates for YdcE. Three compounds (**5**, **7**, and **9**) were identified as substrates, and their steady state parameters are reported in Table 4. The reported kinetic properties for **5** correspond to the rate of formation of the β,γ-unsaturated isomer, 2-oxo-4-pentenoate (**4**, Scheme 1), as there was no detectable rate of formation of the α,β-unsaturated isomer, 2-oxo-3-pentenoate (**6**). The data show that the three compounds have comparable K_m values but differ with respect to their k_{cat} values. Examination of the k_{cat} values indicates that replacing the vinyl group of **5** with a phenyl group results in a modest decrease in catalysis (2.8-fold). However, the addition of a hydroxyl group to the phenyl moiety has a more significant effect on catalysis, and results in a 10-fold decrease in k_{cat}. The values of k_{cat}/K_m parallel the decreases in k_{cat}.

We also examined whether YdcE catalyzed the ketonization of **2** to **3**. 4-OT catalyzes the partitioning of **2**, as well as several related dienols (e.g., **5**), to both the β,γ- and the α,β-unsaturated ketones (*25*). At equilibrium, the α,β-unsaturated isomers (e.g., **3** and **6**) predominate. Our results show that YdcE does not catalyze the formation of **3** (from **2**) or **6** (from **5**). Thus, with these substrates, YdcE strictly catalyzes a tautomerization reaction.

Inhibition Studies of YdcE. On the basis of the observations that YdcE processed **7** and **9**, a substrate analogue of **9**, (*E*)-2-fluoro-*p*-hydroxycinnamate (**11**), was examined as a potential competitive inhibitor. It was found to be a competitive inhibitor with a K_i of 230 ± 20 μM. The crystallographic observations (vide infra) prompted us to examine whether HEPES and benzoic acid also served as potential competitive inhibitors. Both were found to be competitive inhibitors with K_i values of 13.9 ± 2.2 and 3.3 ± 0.4 mM, respectively.

Description of Crystal Structures. Three crystal structures of YdcE have been determined. In each case, the crystallographic asymmetric unit consists of a dimer.[3] A native crystal structure was determined for crystals grown in sodium phosphate buffer. An unambiguous molecular replacement solution was obtained using MOLREP of the CCP4 suite of programs, and the structure was refined to 2.1 Å resolution with crystallographic R and R_{free} values of 22.5 and 26.2%, respectively. The Ramachandran plot shows 92.8% of all non-glycine residues lie within the most favored region and 7.2% lie within the additionally allowed region. The root-

[3] The native molecular mass of YdcE, as estimated by gel filtration chromatography, is 29 400 Da, indicating that the protein is a trimer. This observation is clearly not correct and suggests that YdcE behaves anomalously on a gel filtration column. A similar observation was made for 4-OT (*3*).

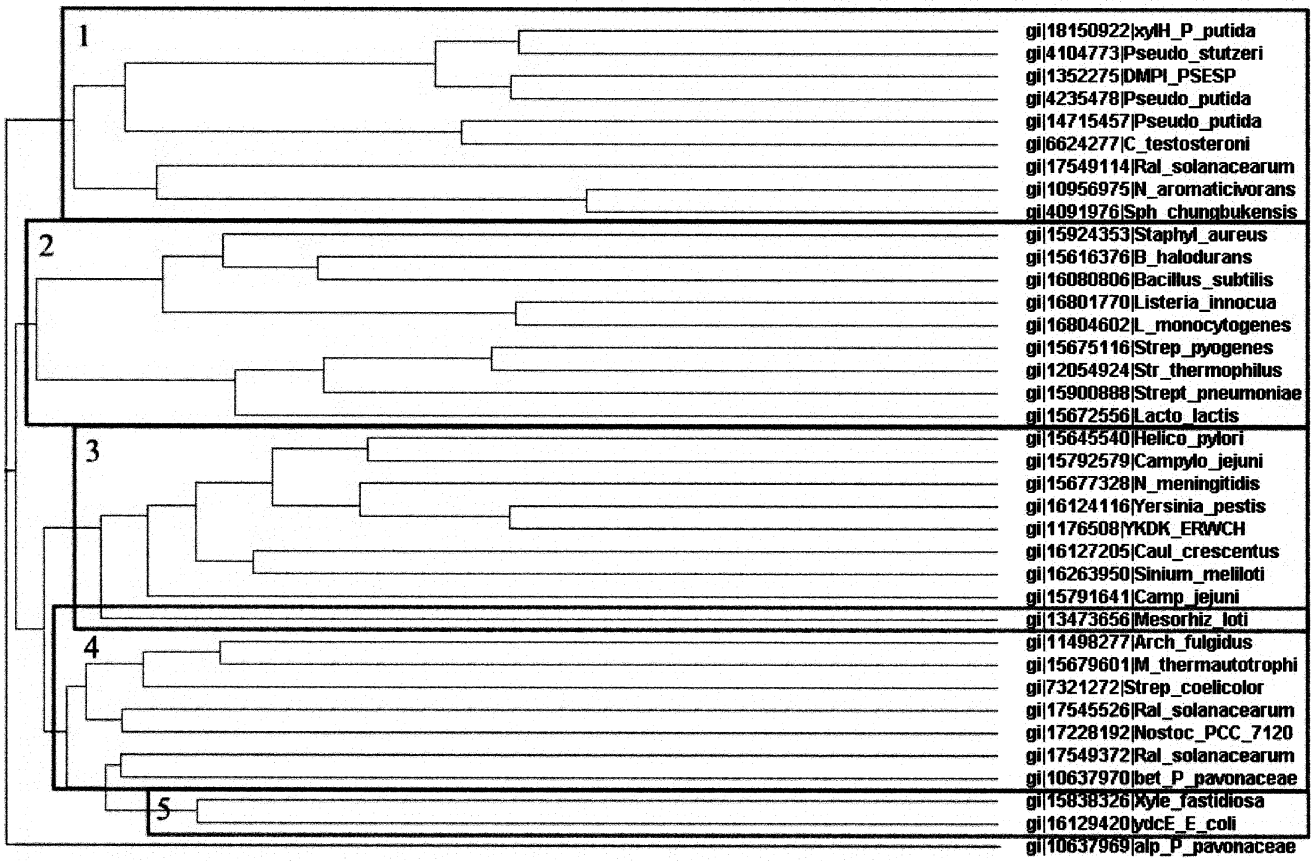

FIGURE 2: Phylogenetic tree of the 4-oxalocrotonate tautomerase family generated using the program PHYLIP (*23*).

mean-square (rms) deviation of Cα atoms residues for the two monomers of this dimer is 0.71 Å.

The crystal structures of YdcE (in HEPES buffer) and the YdcE·**11** complex have been refined against 1.35 Å resolution data to crystallographic R/R_{free} values of 14.2%/16.4% and 15.1%/17.3%, respectively. In both structures, electron density for the polypeptide backbones is well-ordered, with electron density observed for all 76 residues of the monomers. Only residue Glu-11 is observed to lack side chain density beyond Cα, and is therefore modeled as an alanine. Ramachandran plots calculated for these structures show all non-glycine and non-proline residues lie within the most favored regions (96.4%) or additionally allowed regions (3.6%). The rms deviation of the Cα atom between the monomers of the dimer is 0.49 Å for YdcE (in HEPES buffer) and 0.43 Å for the YdcE·**11** complex.

Surprisingly, each monomer of the YdcE crystal structure (obtained from crystals grown in HEPES buffer) contained an unknown and different molecule. Interestingly, both were displaced by **11**. Fortunately, the resolution (1.35 Å) of the data allowed us to identify the two molecules as HEPES (**12**) and benzoate. While the source of **12** is clearly the buffer, the source of the benzoate remains unknown.[4] This structure will be termed the YdcE·HEPES/benzoate complex. The rms deviation for dimers of the native YdcE versus YdcE·HEPES/benzoic acid is 0.65 Å, and 0.61 Å for native YdcE versus the YdcE·**11** complex.

Description of the YdcE Fold. In the YdcE monomer, residues 1−7 comprise β-strand 1 (β-1), residues 8−12 are in a loop connecting β-1 to the first α-helix (α-1, residues 13−32), residues 33−35 are in a loop that connect α-1 to a 3_{10}-helix (residues 36−38), which is followed by a parallel β-strand 2 (β-2, residues 40−46), and then a loop (residues 47−50) connecting β-2 to a second helix (α-helix for residues 51−55 and π-helix for residues 55−60), followed by a turn, and then a third helix (α-3, residues 62−66), and finally a coil conformation for residues 67−76 (Figure 3). In a manner similar to that of 4-OT, the two monomers of YdcE form a dimer such that β-1 and β-2 of one monomer run antiparallel with respect to β-1′ and β-2′ of the second monomer to form a four-stranded β-sheet: ↓β-2, ↓β-1, ↑β-1′, and ↑β-2′. In contrast to 4-OT, β-2 and β-2′ are, in part, stabilized by residues contributed from the C-terminus of monomer′ and monomer, respectively, rather than this interaction coming from the β-hairpin of the neighboring dimer. Specifically, the carbonyl oxygen of Ile-41′ is available to hydrogen bond with the backbone amide nitrogens of Ile-67 (hydrogen bond distance of 2.9 Å) and Lys-68 (hydrogen bond distance of 3.2 Å), while the backbone amide nitrogen of Ile-41′ is within hydrogen bonding distance of the backbone carbonyl oxygen of Lys-68 (2.9 Å). Interestingly, the additional helices of YdcE (α-2 and α-3) are located on the opposite side of the sheet from α-1, and do not make van der Waals contact with α-2′ and α-3′.

[4] One possibility is that the benzoate is the product of an unknown cellular process involving YdcE. An example of such an occurrence comes from a recent report (*37*). The product of the reaction catalyzed by chorismate lyase, 4-hydroxybenzoate, remains bound in the active site of the enzyme. In contrast to benzoate, which binds with millimolar affinity, 4-hydroxybenzoate binds with micromolar affinity.

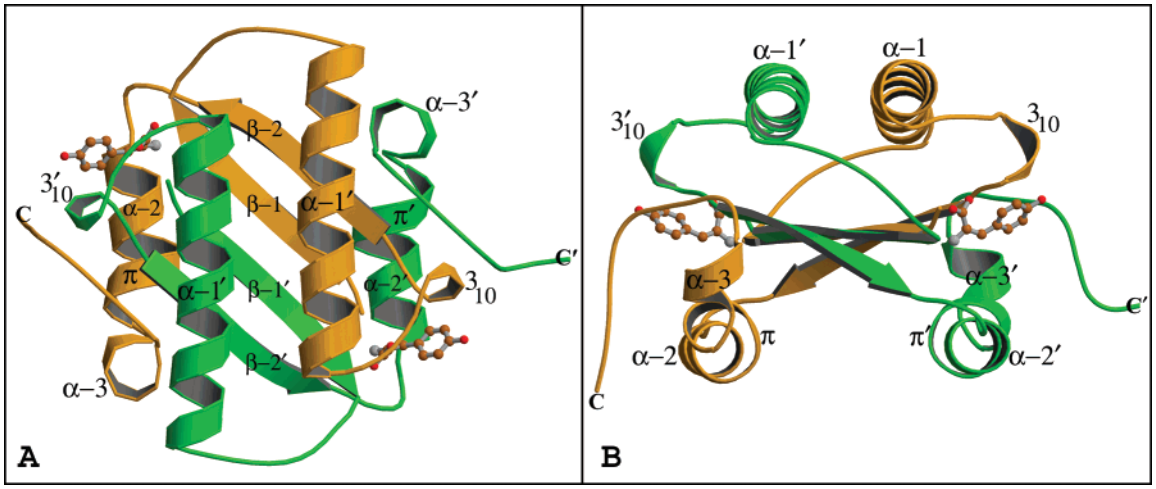

FIGURE 3: Ribbon diagrams depicting the dimeric structure of YdcE. (A) Side view of the YdcE dimer. (B) Top view showing the positions of the additional short helices near the C-terminus. The inhibitor **11** is shown to indicate the location of the two active sites. This figure was prepared using RASTER3D (*5*) and MOLSCRIPT (*6*).

Active Site of YdcE. The crystal structures of the YdcE·**11** complex and the YdcE·HEPES/benzoate complex reveal that the two active sites of the enzyme are located peripherally at the dimer interface (Figure 3). The approximate dimensions of this region are 11 Å × 7 Å × 9 Å. The crystal structures show that the active site is composed of residues contributed from both monomers of the dimer. The phenyl rings of **11** and benzoate and the piperazine ring of HEPES are positioned within a hydrophobic cleft lined by Phe-8′, Trp-51′, and Tyr-72′ (Figures 4 and 5). All three rings are sandwiched between Tyr-72′ and Phe-8′. In addition, there are several other interactions responsible for the binding of these molecules. For the binding of **11**, one carboxylate oxygen of **11** is 2.6 Å from the nitrogen of Pro-1, while the second carboxylate oxygen is located 3.0 Å from the η-nitrogen of the guanidinium group of Arg-10′. The fluoride group is positioned 3.1 Å from the backbone amide nitrogen of Phe-8′. The phenolic hydroxyl group of **11** points toward Tyr-72′, and is within hydrogen bonding distance (2.9 Å) of an ordered water molecule. HEPES and benzoate also form additional interactions with residues within the active site. The binding of HEPES is stabilized further by hydrogen bonding via an oxygen of the sulfonate group to the nitrogen of Pro-1 (3.1 Å), the η-nitrogen of the guanidinium group of Arg-10′ (3.2 Å), and the amide nitrogen of Phe-50′ (3.2 Å) (Figure 5). One oxygen of the carboxylate group of benzoate forms a hydrogen bond with Arg-10′ (3.1 Å), comparable to the interactions observed for the sulfonate group of HEPES and the carboxylate group of **11**.

Inspection of the two active sites of the native YdcE structure reveals few differences in their architecture when compared with those of the two complexes. In all three structures, most side chains of active site residues align with negligible differences. The largest difference is in the repositioning of the aromatic ring of Phe-8, which is rotated approximately 32° in the two complexed structures relative to the native YdcE structure.

The calculation of an electrostatic surface potential map reveals the active site is generally neutral in charge, although the YdcE dimer as a whole exhibits strong electronegative character (calcd pI of 4.7). As observed in the YdcE·**11** structure, the electropositive regions of the active site are attributable primarily to Arg-10′, while the remainder of the active site cleft is formed in part by a hydrophobic region composed of Phe-8′, Trp-51′, and Tyr-72′.

Structural Comparison of the YdcE Monomers. A structural comparison of the two monomers of the native YdcE and those in the YdcE·HEPES/benzoate and YdcE·**11** complexes reveals asymmetry within the dimer. The Cα atoms of the two independent monomers of the native YdcE superimpose with a higher than expected rms deviation of 0.71 Å. The Cα alignment of the four independent monomers of the YdcE·HEPES/benzoate and YdcE·**11** dimers reveals some slight but interesting differences. It is not unexpected to see differences between the two monomers of the YdcE·HEPES/benzoate complex (rmsd of 0.48 Å) because two different ligands are found in the active sites. However, differences of a similar magnitude are also observed between monomers of the YdcE·**11** complex (rmsd of 0.43 Å). Furthermore, there are larger rms deviations between monomers of the same dimer than between the corresponding monomers of different dimers: 0.43 Å rms deviation between YdcE·**11** monomer A and YdcE·**11** monomer B, 0.48 Å rms deviation between YdcE·**12** monomer A and YdcE·**12** monomer B, and 0.13 Å rms deviation between YdcE·**11** monomer A and YdcE·**12** monomer A and between YdcE·**11** monomer B and YdcE·**12** monomer B.

As expected, the largest structural differences occur in the loops of the monomers: loop 1 (residues 8−12), loop 2 (residues 33−35), and loop 3 (residues 47−50). The overall rms deviations are greatest for loop 1 and residues 71−76 of the C-termini. A cross Cα superposition using all 76 residues reveals that the rms deviations of five active site residues (Pro-1, Phe-8, Arg-10, Trp-51, and Tyr-72) are comparable to the overall average (0.34−0.57 Å). Thus, despite very different inhibitors bound to the YdcE active sites, there are relatively few changes in the protein backbone defining the active sites. The largest differences are observed for the Cα of Phe-8 which shifts 0.5 Å in the monomer A active site occupied by HEPES relative to native YdcE monomer A, and shifts 0.7 Å in the monomer B active site occupied by benzoic acid. Furthermore, in the active site of the YdcE·**11** complex, the phenyl ring is rotated by approximately 26° in monomer A and by 30° in monomer B relative to native YdcE.

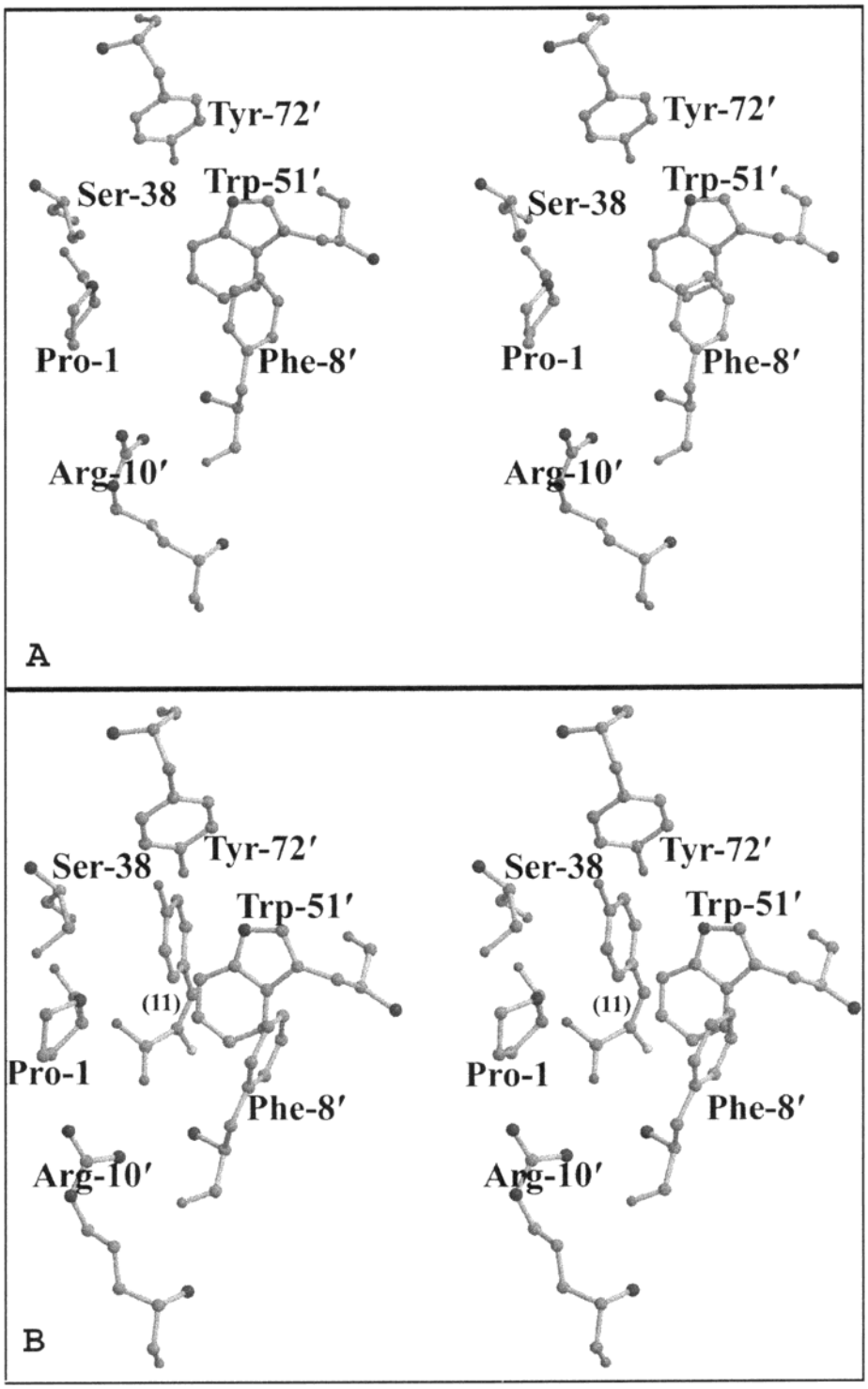

FIGURE 4: (A) Stereodiagram of the active site of native YdcE. (B) Stereodiagram of the active site of the YdcE·**11** complex. The primed residues are from the adjacent monomer. This figure was generated using RASTER3D (*5*) and MOLSCRIPT (*6*).

Structural Comparison of YdcE to 4-OT. 4-OT from *P. putida* and YdcE from *E. coli* share a low degree of pairwise amino acid identity (6%), but conserve the $\beta-\alpha-\beta$ fold of their respective monomers, and the overall architecture of their active sites. The rms deviation of least-squares superpositioned Cα residues A1−50 and B1−50 of the 4-OT dimer (PDB entry 1OTF) and A1−51 and B1−51 of the YdcE dimer is 3.2 Å (Figure 6). The rms deviation values between the two structures are 1.3 Å when loops are eliminated from the calculation and only the α-helices and β-sheets are considered: 1.1 Å for β-1, 1.3 Å for α-1, and 1.4 Å for β-2. The YdcE residues 52−76 were not included in the rms deviation calculation because the C-terminal sequences and structures differ significantly.

Despite the structural homology of their monomers, YdcE and 4-OT differ dramatically in their oligomeric states. 4-OT is a homohexamer, whereas YdcE is a homodimer. Analysis of the 4-OT and YdcE crystal structures reveals structural components that help stabilize their respective oligomeric states. In 4-OT, residues 51−54 (GXGG) contribute to the formation of a β-hairpin turn that is observed to interact with, and extend, the four-stranded β-sheet of an adjacent 4-OT

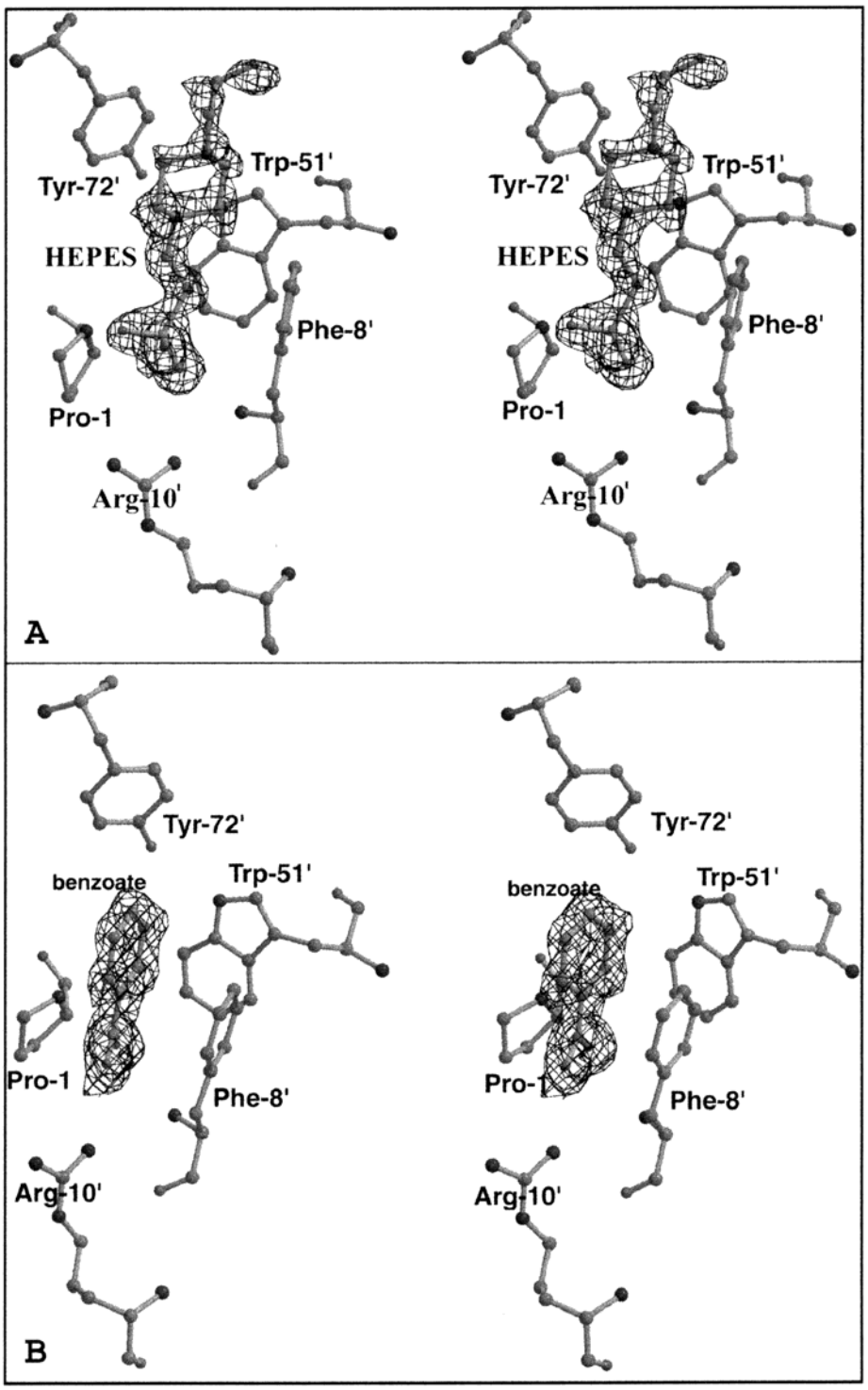

FIGURE 5: (A) Stereodiagram of the active site of YdcE in HEPES buffer showing $2F_o - F_c$ difference electron density observed in active site A with a molecule of HEPES modeled into the electron density. The coordinates for HEPES were omitted from the electron density map calculation. (B) Stereodiagram of the active site of YdcE in HEPES buffer showing the $2F_o - F_c$ difference electron density observed in active site B with a benzoate molecule modeled into the electron density. The coordinates for benzoate were omitted from the electron density map calculation. This figure was generated using RASTER3D (*5*) and BOBSCRIPT (*38*).

dimer in the hexamer. Thus, the β-hairpin turns from one 4-OT dimer stabilize dimers on either side, thereby stabilizing the hexamer of 4-OT (Figure 1D). In contrast, the GXGG β-hairpin sequence and the eight following residues in 4-OT are replaced with 26 residues in YdcE, which form an α-helix, a π-helix, another α-helix, and a coil conformation at the C-terminus of the YdcE monomer. These two occurrences have significant structural implications in the oligomeric state of YdcE. In YdcE, the structural role served by the β-hairpin turns of 4-OT appears to be served by hydrogen bonding between Ile-41 of one monomer and Ile-67 and Lys-68 of the second monomer to stabilize the four-stranded β-sheet of the dimer. Superposition of the conserved $\beta-\alpha-\beta$ parts of YdcE and 4-OT reveals that the helical region in YdcE fills the same space behind the active site as filled by adjacent dimers in 4-OT (Figures 1D and 3).

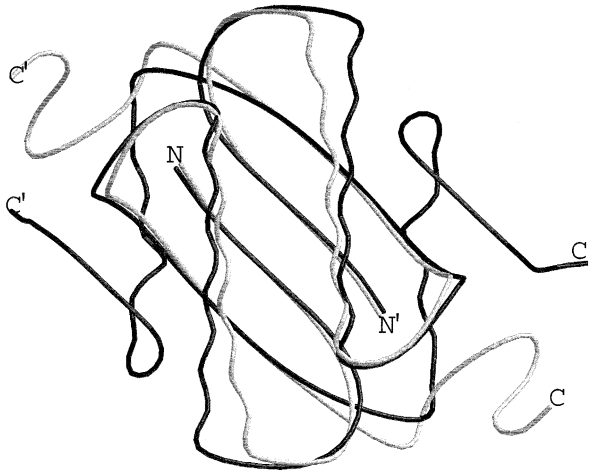

FIGURE 6: Superposition of the backbone traces of 4-OT (gray) and YdcE (black) showing the extensive overlap except for the C-terminal residues. This figure was produced using RASTER3D (*5*) and MOLSCRIPT (*6*).

The key active site residues in 4-OT are Pro-1, Arg-11′, Arg-39″, and Phe-50′ (*10*−*13*), and these elements are largely conserved in the active site of YdcE. The superposition of Cα atoms of 4-OT (residues 1−50) and native YdcE (residues 1−51) (rms deviation of 3.2 Å) shows that the Cα atoms of the prolines differ by 1.3 Å, Arg-11′ and Arg-10′ by 3.1 Å, Phe-50′ and Trp-51′ by 2.3 Å, and Arg-39″ and Tyr-72′ by ∼8.0 Å. Nonetheless, the *η*-nitrogens of the guanidinium groups of Arg-11′ and Arg-10′ differ by only ∼1.8 Å. Additionally, the phenyl ring of Phe-50′ in 4-OT is shifted by only 1.5 Å and an approximately 73° rotation relative to the indole ring of Trp-51′ in YdcE. Finally, the *η*-nitrogen of the guanidinium group of Arg-39″ and the phenolic oxygen of Tyr-72′ differ by ∼2.0 Å. In this respect, the architecture of the two active sites is similar (Figure 7).

A comparison of the electrostatic surface potential of 4-OT and YdcE reveals some striking differences (Figure 8). 4-OT has a relatively neutral surface on the backside of the four-stranded sheet, while this surface is exposed in the YdcE dimer, showing a large electronegative patch, made up predominantly of Glu-58 and Asp-4, located near the molecular 2-fold interface of the dimer. The active sites of the two enzymes also have different electrostatic features. The electrostatic potential surface of the YdcE·**11** dimer (with the inhibitor's coordinates omitted from the calculations) reveals that the molecular surface of the active site is attributable to residues Pro-1, Phe-8′, Arg-10′, Ser-34, Lys-35, Ser-38, Trp-51′, and Tyr-72′. Thus, the active site of YdcE is largely neutral in charge, with some electropositive character being contributed by Arg-10′. In contrast, the active site of 4-OT is formed by residues Pro-1, Ile-2, Arg-11′, Arg-39″, Met-45′, Phe-50′, and Ile-52′, and has electropositive character contributed by Arg-11′ and Arg-39″.

DISCUSSION

When 4-OT was first cloned and overexpressed in 1992, it was thought to be unique because no homologues were identified by sequence analysis (*19*). It was postulated that this apparent uniqueness might be related to its small monomer size (62 amino acids), which was the smallest reported size for an enzyme subunit. This discovery was puzzling in light of the fact that a similar enzyme, 5-(carboxymethyl)-2-hydroxymuconate isomerase (CHMI), was found in *E. coli C* as part of a pathway responsible for the degradation of aromatic amino acids (*40*). CHMI consists of 125 amino acids and catalyzes a reaction identical to that of 4-OT on a structurally similar substrate (the hydrogen at C-5 of **1**−**3** is replaced with a carboxymethyl group).

The mystery was partially solved when the crystal structures of 4-OT and CHMI were determined and found

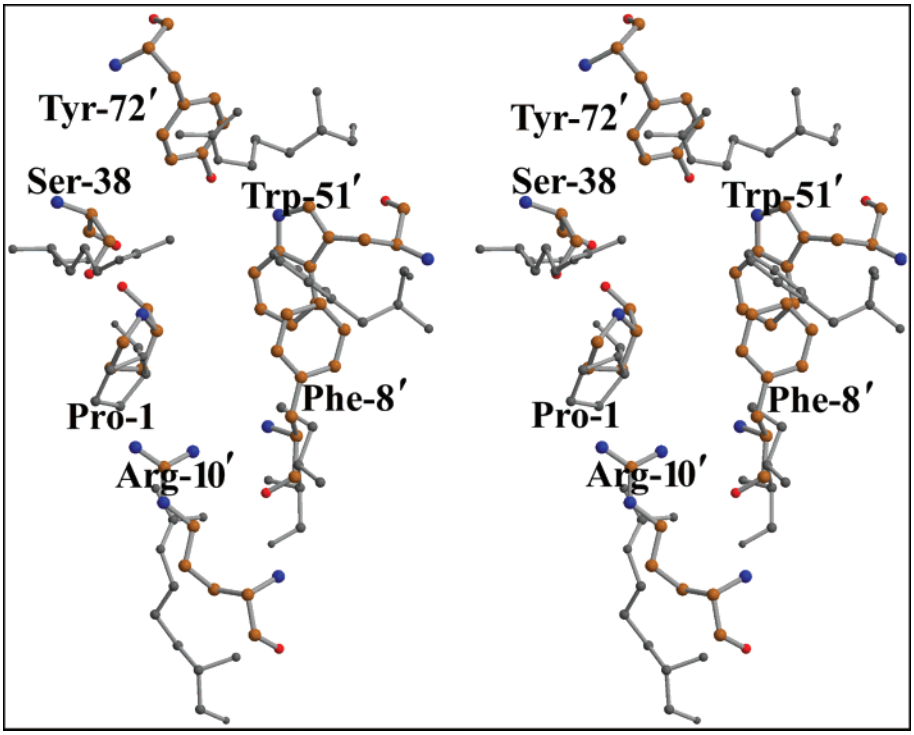

FIGURE 7: Active site superposition of 4-OT and YdcE. The YdcE residues are depicted in color, while the corresponding 4-OT active site residues are represented in gray. This figure was prepared using RASTER3D (*5*) and MOLSCRIPT (*6*).

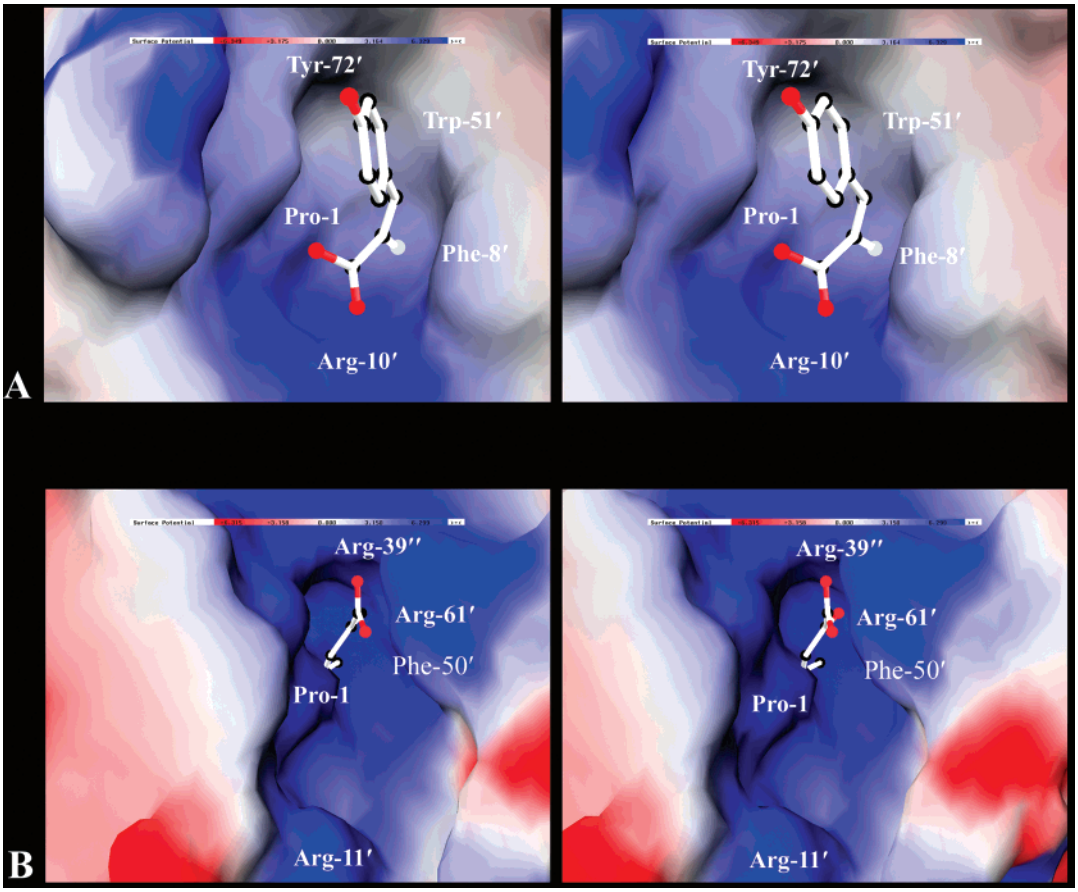

FIGURE 8: Stereodiagrams of electrostatic surface potential representations for the active sites of (A) the YdcE·**11** complex (calculated without the coordinates of **11**) and (B) 4-OT covalently modified by 2-oxo-3-pentenoate (calculated without the coordinates for 2-oxo-3-pentenoate). The adduct was derived by incubating 4-OT and the irreversible inhibitor, 2-oxo-3-pentynoate (*4*). This figure was generated using GRASP (*39*).

to be structurally homologous (*3*). CHMI is a trimer while 4-OT a hexamer, where the CHMI monomer is equivalent to the 4-OT dimer. Both enzymes use the amino-terminal proline as the catalytic base (*7*, *8*, *15*, *40*). Shortly after these crystal structures were reported, the structure of macrophage migration inhibitory factor (MIF), a mammalian cytokine, was determined (*41*). Surprisingly, MIF shared structural homology with both 4-OT and CMHI. MIF consists of 115 amino acids and is a trimer, similar to CHMI. MIF also has a phenylpyruvate tautomerase (PPT) activity, utilizing the amino-terminal proline as the catalytic base (*42*, *43*). On the basis of the conservation of structure and mechanism, these three enzymes were classified as members of the tautomerase superfamily (*44*, *45*).

As a result of the many bacterial genomic sequencing projects, several homologues of 4-OT, CHMI, and MIF have now been identified. The 4-OT homologues range from 61 to 81 amino acids, and are found throughout the bacterial kingdom in common organisms such as *E. coli* and *Bacillus subtilis* as well as thermophiles such as *A. fulgidus*. Many of these organisms are not known to degrade aromatic hydrocarbons, suggesting that these 4-OT homologues have another function in the organism. The assignment of a function is further complicated by two observations: the homologues are not found in known operons, and the genomic context offers no insight about possible functions. Nonetheless, the results reported herein as well as the studies of others (*36*) have uncovered both mechanistic and structural diversity in this family, not previously known.

While the function of these 4-OT homologues is currently unknown, some insight into their substrates can be gained by examining the subfamily classification presented in Table 3. Members of subfamily 1 conserve all the key active site and structural residues of 4-OT and should have very similar structures and substrate specificities. The substrate for 4-OT, **1**, a dicarboxylic acid, interacts with Arg-11 and Arg-39. Subfamily 2 retains Arg-11, but has a histidine (with the exception of YwhB, which has a valine) in place of Arg-39. If the two residues occupy similar positions within the active site cavity, then one possibility is that the members of subfamily 2 accommodate a longer substrate. Arg-39 is absent, while Arg-11 appears only once in subfamily 3. However, this group now displays a conserved lysine at position 33 (using the 4-OT numbering system). Furthermore, this lysine aligns with Lys-32 of MIF, which has been shown to interact with the carboxylate group of PPT inhibitors (*44*), analogous to one of the roles played by Arg-11 in 4-OT. Thus, substrates for subfamily 3 may possess a single carboxylate group, where the other end of the active site is now more hydrophobic due to the replacement of the arginine or histidine at position 39 with a valine or a phenylalanine. Subfamily 4 retains the critical structural residues, but does not conserve any of the active site residues (discussed above) other than Pro-1. The exception to this is the sequence of the α-subunit of the recently characterized *trans*-3-chloroacrylic acid dehalogenase (CaaD), which retains Arg-11. This arginine may play a role analogous to that of Arg-11 in 4-OT and the 4-OT homologues in subfamilies 1 and 2, binding

the carboxylate group and functioning as an electron sink (*36*). Subfamily 4 is not yet fully characterized and may need to be further subdivided pending additional experimental information. For example, both the α- and β-subunits of CaaD are classified in Table 3 as members of subfamily 4. However, on the basis of pairwise alignment scores used to generate the phylogenetic tree (Figure 2), the β-subunit of CaaD is grouped with subfamily 4, but the α-subunit is not grouped with any of the five subfamilies. CaaD is probably a trimer of heterodimers, where the α- and β-subunits presumably have coevolved from a homohexameric ancestor as suggested by the observation that the β-subunit contributes Pro-1 while the α-subunit contributes Arg-11 and Phe-50 to the active site.

The sequence of YdcE is placed in subfamily 5. Thus far, this is the smallest subfamily and is distinguished by the absence of the β-hairpin and the equivalent of Gly-54, which are necessary for hexamer formation. Interestingly, despite the major difference in the quaternary structure and the functional catalytic unit, the active site of YdcE shares two notable similarities with the active site of 4-OT. First, it is composed of residues from both monomers. Pro-1, presumed to be the catalytic base, is from one subunit, while Phe-8, Arg-10, Trp-51, and Tyr-72 are from the other subunit. Second, the structures suggest that the key catalytic residues of the 4-OT family are conserved. In addition to Pro-1, Arg-10 of YdcE takes the place of Arg-11 and Trp-51 replaces Phe-50. A superposition of the structures suggests that Tyr-72 may replace Arg-39.

On the basis of these observations, it is possible to speculate about a possible mechanism for the one activity that has been observed for YdcE, the tautomerization of **5**, **7**, and **9**. If Pro-1 functions as the catalytic base, then it could not interact with one of the carboxylate oxygens of the substrate (as is observed in the three complexes). Thus, the C-1 carboxylate groups of the substrates are likely to form a bidentate interaction with Arg-10 or maintain the observed monodentate interaction with Arg-10 and form an additional interaction with another residue. The structure of the YdcE·**11** complex also shows that the fluoride group interacts with the backbone amide nitrogen of Phe-8′, suggesting that this residue might function as the general acid catalyst. Although Tyr-72 occupies the same space as Arg-39, the general acid catalyst in 4-OT, it does not appear to have a catalytic role in the processing of these substrates. The nonpolar environment of the active site may contribute to a low pK_a for Pro-1, and Trp-51 may play a role in maintaining this environment. This mechanism is clearly speculative and must be investigated further by mutagenesis and structural studies, which are currently underway.

If this mechanism is operative, then it suggests that our understanding of the catalytic strategy used by the members of the 4-OT family is incomplete. For both 4-OT and CaaD, Arg-11 has a role in catalysis and binding (*12*, *36*). Its primary catalytic role is that of an electron sink. In 4-OT, Arg-11 draws electron density to C-5 of **3** (by interacting with the C-6 carboxylate group), which facilitates protonation at this position (*12*). In CaaD, Arg-11 may also draw electron density away from the C-3 position of 3-chloroacrylate, and thereby facilitate nucleophilic attack by water (*36*). In both enzymes, it also serves an additional role in binding the carboxylate group of the substrate. These observations would suggest that Arg-10 in YdcE might behave similarly. However, YdcE is not able to catalyze the conversion of **1** to **3**, indicating that Arg-10 plays a role only in binding of these substrates. This raises the question of whether the dimeric structure of YdcE precludes its ability to convert **1** to **3**. A better understanding of the role of Arg-10 in YdcE, the effect of the oligomer state on catalysis, and the overall catalytic strategy used by the 4-OT family members will be obtained when physiological functions for YdcE as well as the other homologues are identified.

Finally, our crystallographic observations suggest a structural basis for the differences in the potencies of the three inhibitors. The most potent inhibitor, **11**, makes two additional interactions with YdcE, which are not observed for HEPES or benzoate. In addition to the interactions with Pro-1 and Arg-10, the phenolic hydroxyl group of **11** interacts with an ordered water molecule and the fluoride group forms a hydrogen bond with the backbone amide nitrogen of Phe-8. These interactions and any additional hydrophobic interactions between the aromatic ring of **11** and the aromatic rings of Phe-8, Trp-51, and Tyr-72 could account for the almost 60-fold difference in potency between HEPES and **11** and the 14-fold difference in potency between benzoate and **11**.

ACKNOWLEDGMENT

Electrospray ionization mass spectrometry was performed by the analytical instrumentation service core supported by Center Grant ES 07784. We also acknowledge Dr. Steve Ernst and the X-ray facility in the Department of Chemistry and Biochemistry for support of data collection.

REFERENCES

1. Harayama, S., Lehrbach, P. R., and Timmis, K. N. (1984) *J. Bacteriol. 160*, 251−255.
2. Harayama, S., Rekik, M., Ngai, K.-L., and Ornston, L. N. (1989) *J. Bacteriol. 171*, 6251−6258.
3. Subramanya, H. S., Roper, D. I., Dauter, Z., Dodson, E. J., Davies, G. J., Wilson, K. S., and Wigley, D. B. (1996) *Biochemistry 35*, 792−802.
4. Taylor, A. B., Czerwinski, R. M., Johnson, W. H., Jr., Whitman, C. P., and Hackert, M. L. (1998) *Biochemistry 37*, 14692−14700.
5. Merritt, E. A., and Bacon, D. J. (1997) *Methods Enzymol. 277*, 505−524.
6. Kraulis, P. J. (1991) *J. Appl. Crystallogr. 24*, 946−950.
7. Stivers, J. T., Abeygunawardana, C., Mildvan, A. S., Hajipour, G., Whitman, C. P., and Chen, L. H. (1996) *Biochemistry 35*, 803−813.
8. Stivers, J. T., Abeygunawardana, C., Mildvan, A. S., Hajipour, G., and Whitman, C. P. (1996) *Biochemistry 35*, 814−823.
9. Johnson, W. H., Jr., Czerwinski, R. M., Fitzgerald, M. C., and Whitman, C. P. (1997) *Biochemistry 36*, 15724−15732.
10. Czerwinski, R. M., Johnson, W. H., Jr., Whitman, C. P., Harris, T. K., Abeygunawardana, C., and Mildvan, A. S. (1997) *Biochemistry 36*, 14551−14560.
11. Fitzgerald, M. C., Chernushevich, I., Standing, K. G., Kent, S. B. H., and Whitman, C. P. (1995) *J. Am. Chem. Soc. 117*, 11075−11080.
12. Harris, T. K., Czerwinski, R. M., Johnson, W. H., Jr., Legler, P. M., Abeygunawardana, C., Massiah, M. A., Stivers, J. T., Whitman, C. P., and Mildvan, A. S. (1999) *Biochemistry 38*, 12343−12357.
13. Czerwinski, R. M., Harris, T. K., Massiah, M. A., Mildvan, A. S., and Whitman, C. P. (2001) *Biochemistry 40*, 1984−1995.
14. Pirrung, M. C., Chen, J., Rowley, E. G., and McPhail, A. T. (1993) *J. Am. Chem. Soc. 115*, 7103−7110.
15. Whitman, C. P., Aird, B. A., Gillespie, W. R., and Stolowich, N. J. (1991) *J. Am. Chem. Soc. 113*, 3154−3162.
16. Lian, H., and Whitman, C. P. (1993) *J. Am. Chem. Soc. 115*, 7978−7984.

17. Sambrook, J., Fritsch, E. F., and Maniatis, T. (1989) *Molecular Cloning: A Laboratory Manual*, Cold Spring Harbor Laboratory Press, Plainview, NY.
18. Burks, E. A., Johnson, W. H., Jr., and Whitman, C. P. (1998) *J. Am. Chem. Soc. 120*, 7665−7675.
19. Chen, L. H., Kenyon, G. L., Curtin, F., Harayama, S., Bembenek, M. E., Hajipour, G., and Whitman, C. P. (1992) *J. Biol. Chem. 267*, 17716−17721.
20. Waddell, W. J. (1956) *J. Lab. Clin. Med. 48*, 311−314.
21. Altschul, S. F., Madden, T. L., Schaffer, A. A., Zhang, J. H., Zhang, Z., Miller, W., and Lipman, D. J. (1997) *Nucleic Acids Res. 25*, 3389−3402.
22. Thompson, J. D., Higgins, D. G., and Gibson, T. J. (1994) *Nucleic Acids Res. 22*, 4673−4680.
23. Felsenstein, J. (1993) *PHYLIP (Phylogeny Inference Package)*, version 3.5c, Department of Genetics, University of Washington, Seattle.
24. Taylor, A. B., Johnson, W. H., Jr., Czerwinski, R. M., Li, H.-S., Hackert, M. L., and Whitman, C. P. (1999) *Biochemistry 38*, 7444−7452.
25. Lian, H., Czerwinski, R. M., Stanley, T. M., Johnson, W. H., Jr., Watson, R. J., and Whitman, C. P (1998) *Bioorg. Chem. 26*, 141−156.
26. Matthews, B. W. (1968) *J. Mol. Biol. 33*, 491−497.
27. Otwinowski, Z., and Minor, V. (1996) *Methods Enzymol. 276*, 307−326.
28. Collaborative Computational Project, No. 4. (1994) *Acta Crystallogr. D50*, 760−763.
29. Terwilliger, T. C., and Berendzen, J. (1999) *Acta Crystallogr. D55*, 849−861.
30. Perrakis, A., Morris, R. M., and Lamzin, V. S. (1999) *Nat. Struct. Biol. 6*, 458−463.
31. Navaza, J. (1994) *Acta Crystallogr. A50*, 157−163.
32. Guex, N., and Peitsch, M. C. (1997) *Electrophoresis 18*, 2714−2723.
33. Jones, T. A., Zou, J.-Y., Cowan, S. W., and Kjeldgaard, M. (1991) *Acta Crystallogr. A47*, 110−119.
34. Murshudov, G. N., Lebedev, A., Vagin, A. A., Wilson, K. S., and Dodson, E. J. (1999) *Acta Crystallogr. D55*, 247−255.
35. Brunger, A. T., Adams, P. D., Clore, G. M., DeLano, W. L., Gros, P., Grosse-Kunstleve, R. W., Jiang, J., Kuszewski, J., Nilges, M., Pannu, N. S., Read, R. J., Rice, L. M., Simonson, T., and Warren, G. L. (1998) *Acta Crystallogr. D54*, 905−921.
36. Poelarends, G. J., Saunier, R., and Janssen, D. B. (2001) *J. Bacteriol. 183*, 4269−4277.
37. Gallagher, D. T., Mayhew, M., Holden, M. J., Howard, A., Kim, K.-J., and Vilker, V. L. (2001) *Proteins: Struct., Funct., Genet. 44*, 304−311.
38. Esnouf, R. M. (1997) *J. Mol. Graphics 15*, 132−134.
39. Nichols, A., Sharp, K. A., and Honig, B. (1991) *Proteins: Struct., Funct., Genet. 11*, 281−296.
40. Hajipour, G., Johnson, W. H., Jr., Dauben, P. D., Stolowich, N. J., and Whitman, C. P. (1993) *J. Am. Chem. Soc. 115*, 3533−3542.
41. Suzuki, M., Sugimoto, H., Nakagawa, A., Tanaka, I., Nishihira, J., and Sakai, M. (1996) *Nat. Struct. Biol. 3*, 259−266.
42. Rosengren, E., Aman, P., Thelin, S., Hansson, C., Ahlfors, S., Bjork, P., Jacobsson, L., and Rorsman, H. (1997) *FEBS Lett. 417*, 85−88.
43. Stamps, S. L., Fitzgerald, M. C., and Whitman, C. P. (1998) *Biochemistry 37*, 10195−10202.
44. Johnson, W. H., Jr., Czerwinski, R. M., Stamps, S. L., and Whitman, C. P. (1999) *Biochemistry 38*, 16024−16033.
45. Murzin, A. G. (1996) *Curr. Opin. Struct. Biol. 6*, 386−394.

BI020271H